






Article

Effect of the Processing Parameters on the Porosity and Mechanical Behavior of Titanium Samples with Bimodal Microstructure Produced via Hot Pressing

Ricardo Chávez-Vásquez ¹, Sheila Lascano ^{1,*}, Sergio Saucedo ¹, Mauricio Reyes-Valenzuela ¹, Christopher Salvo ², Ramalinga Viswanathan Mangalaraja ³, Francisco José Gotor ⁴, Cristina Arévalo ⁵ and Yadir Torres ⁵

- ¹ Departamento de Ingeniería Mecánica, Universidad Técnica Federico Santa María, Avenida Vicuña Mackenna 3939, Santiago 8940572, Chile; ricardo.chavezv@usm.cl (R.C.-V.); sergio.saucedo@usm.cl (S.S.); mauricio.reyes@usm.cl (M.R.-V.)
 - ² Departamento de Ingeniería Mecánica, Facultad de Ingeniería, Universidad del Bío-Bío, Avda. Collao 1202, Casilla 5-C, Concepción 4081112, Chile; csalvo@ubiobio.cl
 - ³ Departamento de Ingeniería de Materiales, Universidad de Concepción, Edmundo Larenas 270, Concepción 4070409, Chile; mangal@udec.cl
 - ⁴ Instituto de Ciencia de Materiales de Sevilla (CSIC-US), Américo Vespucio 49, 41092 Sevilla, Spain; francisco.gotor@icmse.csic.es
 - ⁵ Departamento de Ingeniería y Ciencia de los Materiales y del Transporte, Escuela Politécnica Superior, Calle Virgen de África 7, 41011 Seville, Spain; carevalo@us.es (C.A.); ytorres@us.es (Y.T.)
- * Correspondence: sheila.lascano@usm.cl



Citation: Chávez-Vásquez, R.; Lascano, S.; Saucedo, S.; Reyes-Valenzuela, M.; Salvo, C.; Mangalaraja, R.V.; Gotor, F.J.; Arévalo, C.; Torres, Y. Effect of the Processing Parameters on the Porosity and Mechanical Behavior of Titanium Samples with Bimodal Microstructure Produced via Hot Pressing. *Materials* **2022**, *15*, 136. <https://doi.org/10.3390/ma15010136>

Academic Editor: Javier Gil

Received: 5 December 2021

Accepted: 23 December 2021

Published: 25 December 2021

Publisher's Note: MDPI stays neutral with regard to jurisdictional claims in published maps and institutional affiliations.



Copyright: © 2021 by the authors. Licensee MDPI, Basel, Switzerland. This article is an open access article distributed under the terms and conditions of the Creative Commons Attribution (CC BY) license (<https://creativecommons.org/licenses/by/4.0/>).

Abstract: Commercially pure (c.p.) titanium grade IV with a bimodal microstructure is a promising material for biomedical implants. The influence of the processing parameters on the physical, microstructural, and mechanical properties was investigated. The bimodal microstructure was achieved from the blends of powder particles with different sizes, while the porous structure was obtained using the space-holder technique (50 vol.% of ammonium bicarbonate). Mechanically milled powders (10 and 20 h) were mixed in 50 wt.% or 75 wt.% with c.p. titanium. Four different mixtures of powders were precompacted via uniaxial cold pressing at 400 MPa. Then, the specimens were sintered at 750 °C via hot pressing in an argon gas atmosphere. The presence of a bimodal microstructure, comprised of small-grain regions separated by coarse-grain ones, was confirmed by optical and scanning electron microscopies. The samples with a bimodal microstructure exhibited an increase in the porosity compared with the commercially available pure Ti. In addition, the hardness was increased while the Young's modulus was decreased in the specimens with 75 wt.% of the milled powders (20 h).

Keywords: porous titanium; bimodal microstructure; hot-pressing; powder metallurgy; mechanical milling; mechanical behavior

1. Introduction

The research field related to biomedical materials has been grown in recent decades as a result of the demand for implants for bone replacement [1]. Titanium and its alloys are considered the most suitable option for biomedical applications due to their low density, high biocompatibility, specific mechanical strength, and corrosion resistance, as well as their in vitro and in vivo acceptable behavior [2,3]. However, there is mismatch between the stiffness of bone and metallic biomaterials. This incompatibility generates the stress-shielding phenomenon which promotes bone resorption at the implant–bone interface and can even induce implant failure [4,5].

It is well known that porous structures exhibit lower elastic modulus than their fully-dense counterparts [3,6]. It has also been identified that titanium components that

possess optimal macro/micro porosities allow for the tuning of the elastic modulus in a considerably wide range, which also favors bone cell ingrowth and vascularization [3].

Among the manufacturing processes employed to obtain porous metallic materials are tied freeze casting [7,8], selective laser melting (SLM) [9,10], field assisted sintering (FAST) [11,12], and powder metallurgy [13,14]. Powder metallurgy, in combination with the space-holder technique, represents a cost-effective and flexible way to obtain components with a high-degree of porosity (35–80%) and a homogeneous distribution of pores throughout the volume [15–17]. Particles commonly used as space-holders include NH_4HCO_3 [5,18–22], NaCl [17,18,21,23,24], starch [25,26], Mg [27–29], PMMA [30,31], saccharose crystals [26,32], PVA [33], and carbamide [15,34,35], which can be eliminated at a relatively low temperature, or can be easily removed by a dissolution process, generally in water [3]. NH_4HCO_3 is one of the preferred spacer particles due to its moderate decomposition temperature, which makes it easily and completely removable, ensuring a low uptake of impurities such as oxygen, nitrogen, and carbon [17].

However, although this increase in porosity leads to a reduction in Young's modulus, it also reduces mechanical strength. Previous work [36] has shown that, to obtain Young's modulus close to that of human bone, porosity percentages greater than 45% are required. This leads to a drastic reduction in mechanical resistance, below what is required for bone replacement [17,36,37].

Concerning the mechanical performance, titanium components that exhibit a fine grain structure have gained attention due to the grain boundary strengthening effect [38,39], which results in an important increase in strength and hardness when compared to their coarse-grained counterparts. However, regardless of the processing methods, fine-grained metallic materials usually suffer from poor plastic deformation at room temperature [40]. An approach based on tailoring the microstructure by the development of bimodal/multimodal grain size distributions has been implemented, aiming to optimize the balance between ductility and strength [41,42]. Thus, fine grains provide a strength increase, while coarse grains allow ductility to be retained [43]. This method presents the potential to produce materials with a porous structure and suitable combination of elastic modulus, strength, and ductility, which allows an adequate balance between biological and mechanical behavior for biomedical applications.

In recent investigations, titanium samples with a bimodal microstructure synthesized by spark plasma sintering (SPS) have shown yielding stress and ultimate tensile strength values that exceeded twice the value of conventional α -titanium coarse-grained components [44] and hardness that exceeded the nominal value of commercially pure (c.p.) titanium by 3–4 times [45]. Hot consolidation techniques, such as hot pressing sintering (HP) [46], hot isostatic pressing (HIP) [47], and SPS [45], allow the fabrication of components with bimodal structure due to their characteristics of rapid heat/cooling rates and low sintering temperatures, which limits the excessive grain growth preserving the fine-grained microstructure when compared to the conventional sintering processes [48,49]. Besides, it has also been shown that HP increases the chemical homogeneity of the phases present in titanium alloys, and effectively controls grain growth in their microstructure [50,51]. However, the formation of porous structures, which is essential for Ti implants, by pressure-assisted techniques is rather complicated. To circumvent this problem, the use of the space-holder methodology is proposed in this work.

Therefore, the aim of this research is to obtain porous samples of titanium with bimodal microstructure via powder metallurgy from blends of powder particles with different sizes, using NH_4HCO_3 as a temporary spacer particle, and consolidated by hot pressing. The effect of the processing parameters on the bimodal microstructure, porosity, and microhardness of titanium samples is studied.

2. Materials and Methods

2.1. Starting Materials Preparation and Characterization

C.p. titanium grade IV was used as raw powder to produce the bimodal microstructure. According to the supplier's information (Alfa Aesar, Tewksbury, MA, USA), the mean particle size was less than 45 μm . In order to form the bimodal microstructure, the size and morphology of titanium powders were modified by mechanical milling in a planetary mill RETSCH[®] PM 400 (Retsch, Haan, Germany). Thus, 20 g of titanium powder, ZrO₂ (YSZ) ceramic balls with 5 and 10 mm of diameter (ball to powder weight ratio 10:1), and a 2 wt.% of stearic acid as processing control agent (PCA) were placed in a 250 cm³ ZrO₂ vial. One of the studied parameters was the influence of milling time over the obtained bimodal microstructure; thus, the milling was done using two effective milling times: 10 and 20 h. The milling procedures were carried out at 250 rpm, in cycles of milling and resting of 30 min, in argon atmosphere (ultrapure with <3 ppm O₂) to prevent excessive heating and the oxidation of the powder, respectively. From here, the resulting powders are named Ti₁₀ and Ti₂₀.

Regarding the amount of fine powder, two different blends of powders were established: 50 wt.% and 75 wt.% of milled powder, where the remaining percentage corresponds to the as-received Ti powder. The processing parameters were chosen in order to detect improvements related to the capability of retaining porosities, although the high densification technique and the mechanical properties achieved this due to the hardening effect during milling stage. Table 1 summarizes the powder parameters used in order to produce each blend. Hence, the four blends are named Ti₁₀₋₅₀, Ti₁₀₋₇₅, Ti₂₀₋₅₀, and Ti₂₀₋₇₅.

Table 1. Powder parameters for blend processing.

Milling Time (h)	Nomenclature	Portion of Milled Powder (wt.%)	Nomenclature
10	Ti ₁₀	50	Ti ₁₀₋₅₀
		75	Ti ₁₀₋₇₅
20	Ti ₂₀	50	Ti ₂₀₋₅₀
		75	Ti ₂₀₋₇₅

Before the consolidation stage, morphological analysis of starting powders and NH₄HCO₃ particles was carried out by Scanning Electron Microscopy (SEM) with a JSM-6380LV SEM JEOL (JEOL Ltd., Tokyo, Japan) microscope equipped with an Energy Dispersive X-Ray Spectroscopy (EDS) device, according the ASTM F1877 [52] standard. A particle size analysis of the milled and as-received Ti powders were performed using laser diffraction analysis in an Analysette 22 (Frisch GmbH, Idar-Oberstein, Germany) equipment, whereas the granulometric test of NH₄HCO₃ study was accomplished by sieving on an SS3 Gilson[®] (Gilson Incorporated, Global Headquarters, Middleton, WI, USA) device, according to ASTM E2651 standard [53]. Furthermore, X-ray diffraction (XRD) analysis was performed on the as-received and milled (Ti₁₀ and Ti₂₀) powders. The XRD patterns were obtained with STOE STADI MP (STOE & Cie GmbH, Darmstadt, Germany) using CuK α 1 radiation ($\lambda = 0.15406$ nm) and a step size of 0.12 $^\circ$; the scan was recorded in the 2 θ range comprised from 20 $^\circ$ to 120. Once the starting powders were characterized, the specimens were consolidated in order to study the effect of the processing parameters on the final properties of the sintered samples.

2.2. Green Specimens Preparation and Hot Consolidation

Before consolidation of specimens, powder blends (Table 1) and NH₄HCO₃ (50 vol.%) particles were mixed for 40 min in a TURBULA[®] T2F (WAB, Muttenz, Switzerland) to reach good homogenization. The amount of prepared mixture was established regarding the final dimensions of the specimens, having a cylindrical geometry with a diameter of 12.7 mm and height of 20 mm, according to ISO 13314 [54] and ASTM E9 [55] standards.

Next, uniaxial cold compaction of mixtures was performed in a universal testing machine Zwick/Roell Z100 (Zwick/Roell, Ulm, Germany) in two stages. The first one was at a compaction pressure of 20 MPa (3 mm/min) and the second one at 500 MPa (5 mm/min), using 2 min dwell time and 15 min unloading time.

Subsequently, specimens were sintered in a hot press HP20-4560-20 (Thermal Technology LLC, Santa Rosa, CA, USA) in two stages: first, at 100 °C for 1 min in vacuum (10^{-2} mbar), and then at 750 °C and 15 MPa pressure for 15 min in an argon atmosphere (heating rate in both stages was 10 K/min). A graphite die was used, previously coated by a boron nitride-sprayed film to avoid direct contact between the die and the green specimen. The first stage was performed to remove impurities and humidity, and to start the elimination of the space-holder particles, and the second one to continue removing remnants of the spacers and to sinter the green specimens. After sintering, the titanium samples were ground to remove the boron nitride residues. Then, the samples were characterized in order to study the microstructural aspects, porosity, and mechanical properties achieved after the sintering stage.

2.3. Microstructural and Mechanical Characterization of Sintered Samples

The specimens were prepared for microstructural analysis and microhardness measurements by conventional steps of metallographic preparation, according to ASTM E3 [28], with a final step consisting of a mechanical-chemical polishing using colloidal silica and hydrogen peroxide.

Size, morphology and porosity distribution, pores roughness, and bimodal microstructure were analyzed by image analysis (IA) of the micrographs obtained by optical microscopy (OM) in a Nikon Eclipse MA100N (Nikon Corporation, Tokyo, Japan) microscope, and by SEM in a Quanta FEG-250 SEM (Thermo Fisher Scientific, Waltham, MA, USA). IA was performed using Image Pro Plus software. The evaluated and studied porosity parameters were: (i) total porosity ($P(IA)$), (ii) equivalent diameter of pores (D_{eq}), and (iii) pore shape factor ($F_f = 4\pi A / (PE)^2$), where A is the pore area and PE is its perimeter. An F_f value close to 1 suggests a rounded pore, while a value close to 0 suggest a needle-shaped pore.

An analysis of variance (ANOVA) was carried out by a Tukey's test using Statgraphics® software, considering a significance level of $p < 5\%$.

The microhardness measurements were performed in an HMV-G (Shimadzu, Kyoto, Japan) tester, applying a 98.07 mN load for 10 s.

Young's modulus, E_p , was estimated by the Nielsen's equation [56], expressed as follows:

$$E_p = E_{Ti} \times \left[\frac{\left(1 - \frac{P(IA)}{100}\right)^2}{1 + \left(\frac{1}{F_f} - 1\right) \frac{P(IA)}{100}} \right] \quad (1)$$

where, E_{Ti} is the Young's modulus for c.p. Ti grade IV bulk (~110 GPa [57]), $P(IA)$ is the percentage of total porosity of the sample, and F_f is the shape factor calculated from the results of the image analysis.

In addition, the yield strength values were assessed from the correlation proposed by Jha et al. [58], expressed as follows:

$$\sigma_{y,f} = 0.74 \times \sigma_{y,b} \left(\frac{\rho_f}{\rho_b} \right)^{2.206} \quad (2)$$

where, σ_y is the yield strength, ρ is the material's density, and the subscripts f and b are for the porous and bulky material, respectively. The density values were estimated from the measured values of mass and volume of sintered specimens, and the yield strength and density of Ti used were the ones provided by the raw material supplier. This is a preliminary approach to estimate the yield strength due to the employed model and did not consider the effect of bimodal microstructure.

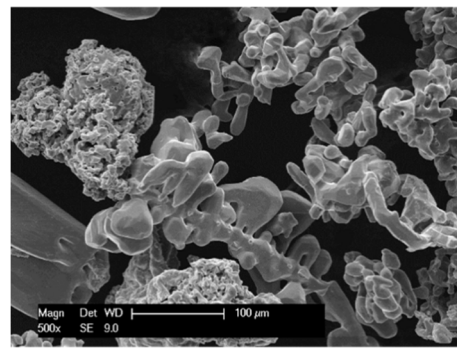
3. Results and Discussion

3.1. Characterization of Starting Materials

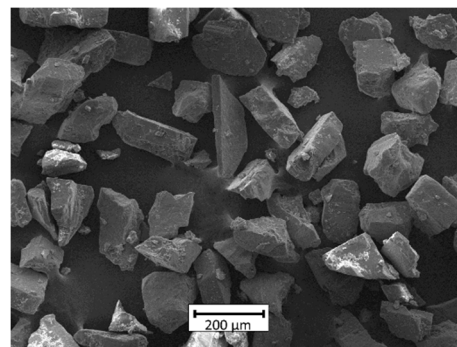
The results of the morphological analysis of the starting powders by SEM images and the particle size distribution, obtained by laser diffraction analysis, are depicted in Figure 1. The SEM images of the as-received titanium powders are shown in the Figure 1a, where an irregular shape is appreciated, typically from its processing via hydrogenation/dehydrogenation. The mean particle size is 50 μm in a range of 10–100 μm (Figure 1e). NH_4HCO_3 particles, Figure 1b, exhibit a polygonal and cubic morphology with a high dispersion of particle size. Particle size distribution of spacer present a normal distribution with a particle size between 50 μm and 400 μm (Figure 1); this distribution was the result of the sieving stage performed during preparation. Some investigations have shown the relevance of spacer particle size and morphology to generate a structure where the total porosity is controlled in an appropriate manner [17,36,59].

Morphologies and the particle size of milled titanium powders, after 10 h (Ti_{10}) and 20 h (Ti_{20}), are presented in Figure 1c,g and Figure 1d,h, respectively. In the case of milled Ti, a reduction in particle size and changes in the particle size distribution are obtained as a consequence of the mechanical milling. A mean particle size of 10 μm in the range between 3 and 70 μm was confirmed for Ti_{10} and a bimodal distribution was evidenced for the Ti_{20} with two mean sizes: 15 μm in the 3–30 μm range, and 0.6 μm in a range of 0.2–2 μm . Despite the increase in milling time, the mean particle size of the main distribution of Ti_{20} powders was larger than that of the Ti_{10} powders. This is due to the fact that, in the initial stage of milling, the dominant phenomenon is fracture, whereas, after increasing milling time, the active phenomena are fracture and cold welding [60], which results in an agglomeration of particles and the formation of two distributions for the Ti_{20} powders. This phenomenon has been recognized as the final stage of the particle–particle interactions in dry-milling processes [61].

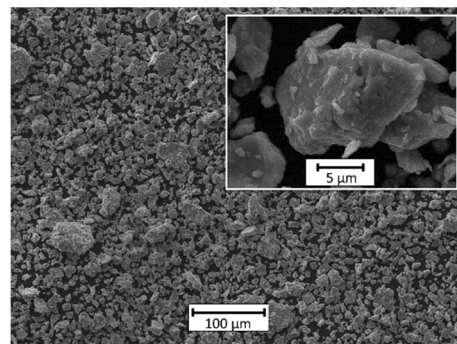
The XRD patterns of the as-received and milled Ti powders are shown in Figure 2, providing structural information. In the case of the as-received powder, only diffraction peaks that correspond to the Ti-hcp phase were detected. On the other hand, both milled powders (Ti_{10} and Ti_{20}) exhibited the Ti-hcp peaks, accompanied by several peaks and a “hump” visualized as $2\theta = 35^\circ - 42^\circ$. The Ti-hcp peaks of both milled powders are broader in shape than the Ti-hcp peaks of the as-received powders, which suggest that, after milling, the crystallite size of this phase may decrease. This effect is frequently observed in high-energy milled powders due to the continuously welding and fracture processes occurring between them during the process [62]. Studying the pattern of both milled powders in detail, the diffraction peaks of Ti- γ were identified (in $2\theta = 36.2^\circ$, 42.1° , and 61.2°), which is a metastable phase (FCC) with the Fm3m space group, which should not be confused with the Ti- β phase, which is also a cubic structure (BCC) but has an Im3m space group and should have diffraction peaks in $2\theta = 38.5^\circ$, 55° , and 69° , peaks that are missing in the pattern. It has been reported that the formation of this metastable phase by ball-milling is driven by the accumulation of partial dislocations and stacking faults induced by high plastic deformation and nanocrystalline grain size [63–67]. In addition, the presence of diffraction peaks of YSZ is associated with the contamination that comes from the milling media.



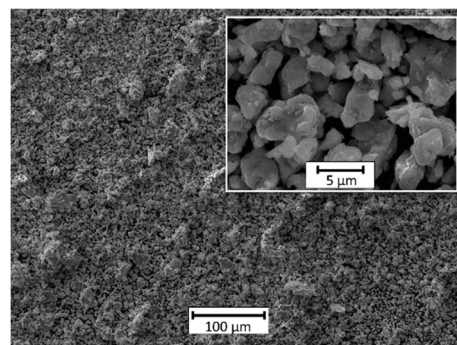
(a)



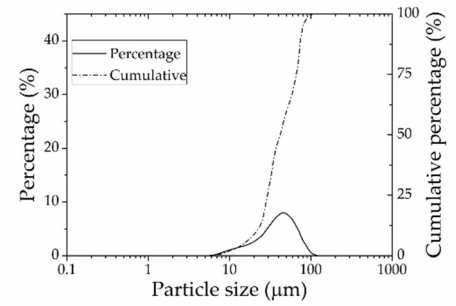
(b)



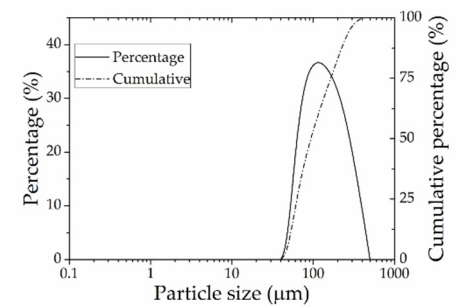
(c)



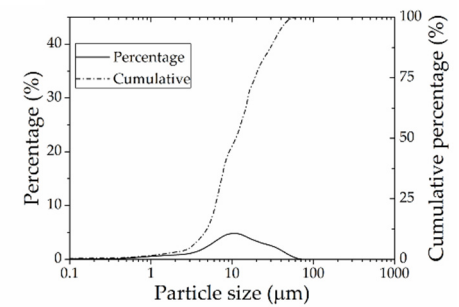
(d)



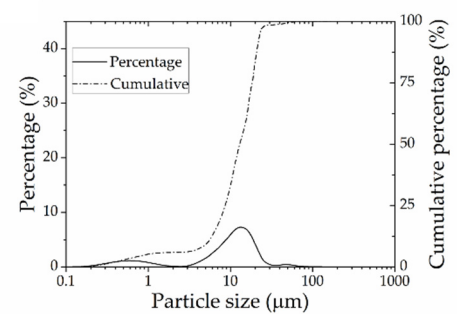
(e)



(f)



(g)



(h)

Figure 1. SEM images of: (a) as-received titanium powders; (b) NH_4HCO_3 particles; (c) Ti_{10} milled powder; (d) Ti_{20} milled powder. Particle size distribution of: (e) as-received titanium powder; (f) NH_4HCO_3 particles; (g) Ti_{10} milled powder; (h) Ti_{20} milled powder.

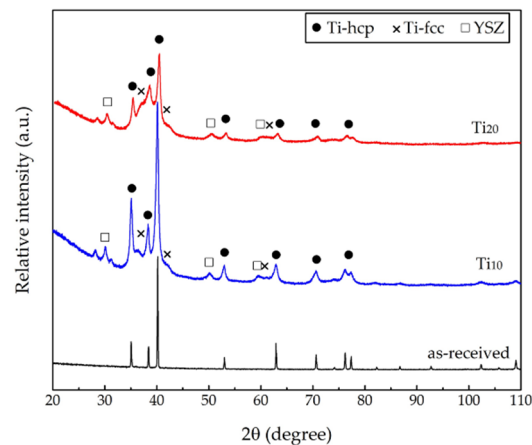


Figure 2. XRD patterns of titanium powders: as-received (black), Ti₁₀ (blue), and Ti₂₀ (red).

3.2. Microstructural Characterization of Sintered Samples

The results from the optical microscopy of the obtained samples are shown in Figure 3. Figure 3a represents an optical microscopy of the c.p. Ti specimen with 50 vol.%. In this sample, a titanium matrix with a very low porosity is observed, with isolated pores with sizes close to 20 microns. According to the results, the porosity is well below that obtained with the conventional powder metallurgy technique, where 50% spacer generates porosities between 40% and 45% [59]. However, as indicated in Table 2, the porosity obtained is less than 2%. This means that hot pressing has eliminated both the spacer and the porosity that it could have generated, so that it would not be named a “metal foam” with a final porosity of 45–60% pores. In addition, in Figure 3b–e, the micrographs of the Ti₁₀ and Ti₂₀ samples are shown, respectively. In general, a porous matrix with a bimodal microstructure, with higher porosity compared to the c.p. Ti, is observed. The addition of spacer particles and milled powders promotes a porous structure that exhibits irregular pores with rounded borders. These pores reach a mean size of between approximately 40 and 250 μm , and they are surrounded by a fine-particle structure; pores with a lower size are homogeneously and randomly distributed throughout the titanium matrix. It is observed that the porosity percentage goes up as the milling time and the percentage of milled powders increase. It can be stated that porosity depends equally on both factors. An increase in the pore size with the milling time is also noticed, where the maximum pore sizes were achieved for those samples that contain the Ti₂₀ powder. In addition, the porosity in the sample was affected by the amount of milled powder used to produce the bimodal microstructure, where the small pores go up when the milled powder percentage increases.

Table 2. Morphological parameters of pores.

Sample Name	P(IA) (%)	D_{eq} (μm)	F_f
Ti ₁₀₋₅₀	1.5 \pm 0.4	84 \pm 8	0.70 \pm 0.16
Ti ₂₀₋₅₀	12.5 \pm 3.8	121 \pm 6	0.75 \pm 0.11
Ti ₁₀₋₇₅	13.2 \pm 0.4	100 \pm 4	0.75 \pm 0.07
Ti ₂₀₋₇₅	35.5 \pm 1.5	141 \pm 4	0.80 \pm 0.09

The differences in pore size could be a consequence of the particle size distribution of the used powders. In this sense, it is possible that smaller particles were used to redistribute its mass to larger particles [68]. If a small particle forms a neck with large particles and redistributes its mass with them, and these large particles were restricted in movement together (as is the case when surrounded by denser regions), then the smaller particle would break away (de-sinter) from one of the larger particles and be absorbed by the other. In consequence, pore growth takes place to reduce the surface to volume ratio of a powder compact when the compact is restricted from shrinking, as is the case for

the bimodal microstructure, where pore growth occurs in regions where densification is locally restricted by the denser zones (unmilled powders), although these partially dense zones are globally subjected to densification particles [68]. Furthermore, it is known that agglomerates have a strong influence on densification because they prevent the effective transfer of heat and pressure to the particles during sintering [69–72]. Another de-sintering cause in the powder compact could be the presence of inclusions [73]. This behavior could be caused by the contamination of the ground powders during the milling process, caused by the release of ZrO_2 from the milling medium. This lack of sintering is related to the fact that these contaminants are refractory materials [74]. Furthermore, the oxide content in the milled powders hinders the particle–boundary motion of coarse particles during sintering, hereby lowering the particle coalescence [75].

Backscattering Electron–SEM images (BSE–SEM) of sintered samples are shown in Figure 3f–j, where the microstructure of the titanium sample (Figure 3f) was compared with those compacts prepared from the mixed powders (Figure 3g–j). On one hand, in the sample of pure titanium with 50 vol.% NH_4HCO_3 (Figure 3f), a typical microstructure of c.p. Ti with equiaxial grains and some micropores in the matrix was observed. However, the spacer and the pores, which should have been generated from it, had disappeared due to the densification action of the HP process. On the other hand, the samples prepared from the mixed powders exhibited a bimodal particle microstructure consisting of coarse and fine grains, where the bimodal microstructure can be identified by the presence of clusters of microporosities, which are caused by the fine particles. The coarse particles that originate from the unmilled powders are randomly distributed and surrounded by porous regions with fine particle microstructure. The porosity of compact prepared from the mixed powders is higher than that observed in the c.p. Ti samples (Figure 3a,f). The porosity increases as the amount of milled powder and milling time increases. It should be noticed that only in Ti_{20-75} could the observed porosity values correspond to a porosity close to that added by the spacer. Relatively large pores in the order of 250 microns are observed in this sample (Figure 3e), but also small pores left by the spacer, as seen in Figure 3f. This figure presents and describes the surface of a pore caused by the spacer with a relatively small size, but it is also possible to distinguish the bimodal microstructure.

Interesting aspects about the bimodal microstructure and porosity in Ti_{20-75} samples are presented in Figure 4. The bimodal microstructure is evenly distributed throughout the entire specimen (Figure 4a), which indicates that a good homogenization was achieved during the mixing process. Three zones were identified in the samples (Figure 4b) as follows: (i) Zone A: fine particles zone, where the milled powders are predominant, surrounding a coarse particle zone (Zone B); (ii) Zone B: coarse particle zone, promoted by unmilled powders; (iii) Zone C: an intermediate or mixed zone with both fine and coarse particles. The formation of the three zones can possibly be attributed to assembly mechanisms between the powder particles, forming clusters through agglomeration. Although different mechanisms lead to the agglomeration of particles in a sample, in this case, the agglomeration could occur during mechanical milling and even blending, where the particles collide and can stick together as a result of completely random movement within the confined space such as the grinding vessel or mixing vessel [76]. The agglomeration of the particles by size was observed in the particle size distributions for the titanium ground at 10 h and 20 h (Figure 1g,h). Another mechanism that can carry out the agglomeration of the particles during these milling or mixing events is known as gravitational agglomeration, which depends on the size of the particles and their speed, where the particles that settle slower are trapped by those that settle faster [76]. The latter may explain the mixed zone (Zone C, Figure 4). In addition, the matrix composition in the different zones present in the bimodal microstructure was evaluated by EDS analysis. The presence of ZrO_2 is detected in Zones A and C, comprised by milled powders, which is the result of the contamination of the milling media.

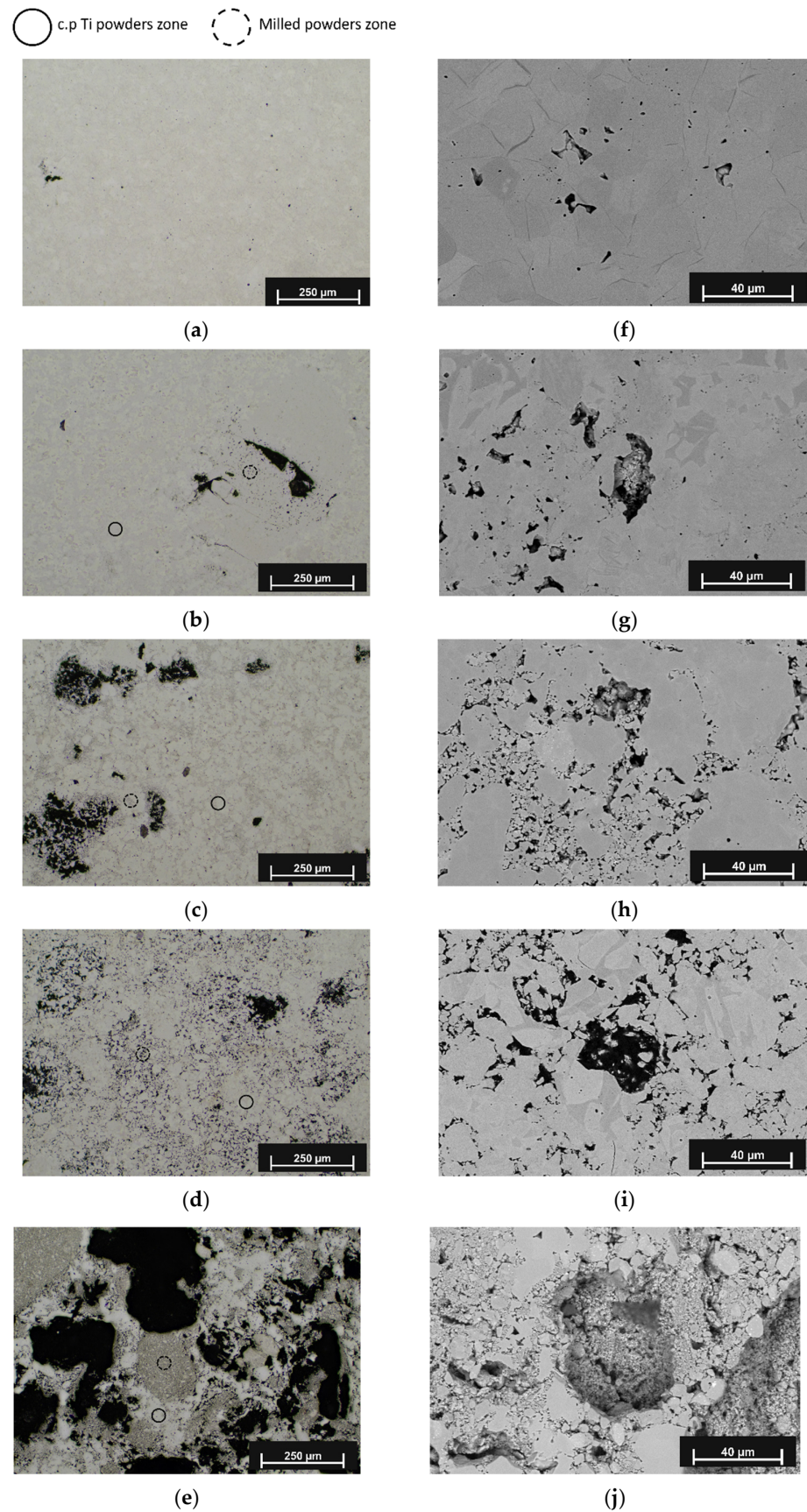


Figure 3. Optical micrographs of Ti samples: (a) c.p. Ti; (b) Ti₁₀₋₅₀; (c) Ti₂₀₋₅₀; (d) Ti₁₀₋₇₅; (e) Ti₂₀₋₇₅; BSE-SEM images of Ti foams: (f) c.p. Ti; (g) Ti₁₀₋₅₀; (h) Ti₂₀₋₅₀; (i) Ti₁₀₋₇₅; (j) Ti₂₀₋₇₅.

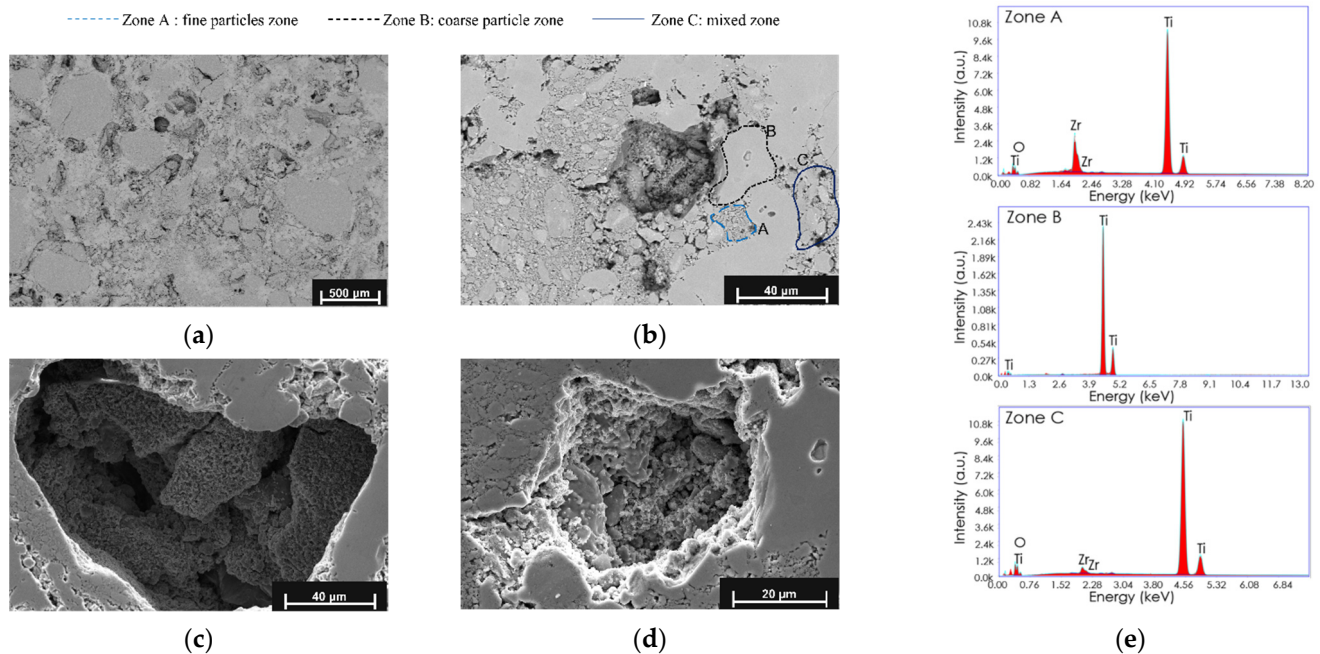


Figure 4. Microstructural aspects of synthesized Ti_{20-75} specimen: BSE-SEM images (a) general view of bimodal microstructure; (b) characteristic microstructure of sample with three zones: Zone A—fine particles; Zone B—coarse particle; Zone C—mixed zone. SE-SEM images (c) Macro-pore surface; (d) Micro-pore surface; (e) EDS analysis for the different zones present in bimodal structure: Zone A, Zone B, and Zone C.

Two types of porosity were distinguished, as is observed in the Secondary Electron-SEM (SE-SEM) images shown in Figure 4c,d: the porosities were promoted by the spacer particles with a pore size of around $100\ \mu\text{m}$, a rough surface, rounded borders, and were interconnected (Figure 4c), and the porosities inherent to the powder metallurgy process with a pore size of around $10\text{--}50\ \mu\text{m}$ and a rough surface were surrounded by the Zones A and B (Figure 4d).

The results of image analysis are summarized in Figure 5, where the stacked frequency distribution histograms of the pore size for each of the consolidated specimens are presented. Each bar of the histograms represents a quantity of pore counts with size in the comprised range. It is important to remember that all of the study samples in this graph have a 50% spacer added. The objective, then, is to evaluate the effect of the amount of ground powder and the grinding time on the pore size and on the porosity that could be obtained despite the use of the HP process. This figure shows the accumulated pore size corresponding to spacers with significant amounts of sizes between 100 and 150 microns, where it is possible to observe that specimens with higher amounts of fine powders (Ti_{10-75} and Ti_{20-75} , Figure 5b) show higher frequencies of larger pores. The mentioned effect on porosity is observed in Figure 3d,e, where there are bigger pores in specimens using 75 wt.% of milled powders. A similar behavior has been documented by Dirras et al. [75], who produced Ni samples using different particle sizes and observed a “shielding effect” by introducing coarse particles onto a fine-particle matrix because the coalescence of coarse particles was hindered.

In addition, the pore size distribution shows that the samples Ti_{10-50} and Ti_{10-75} (10 h of milling time) exhibit porosities up to $200\ \mu\text{m}$, while the samples with the Ti_{20} powder have 80% of its total porosity in this range, and the remaining 20% is between 200 and $400\ \mu\text{m}$.

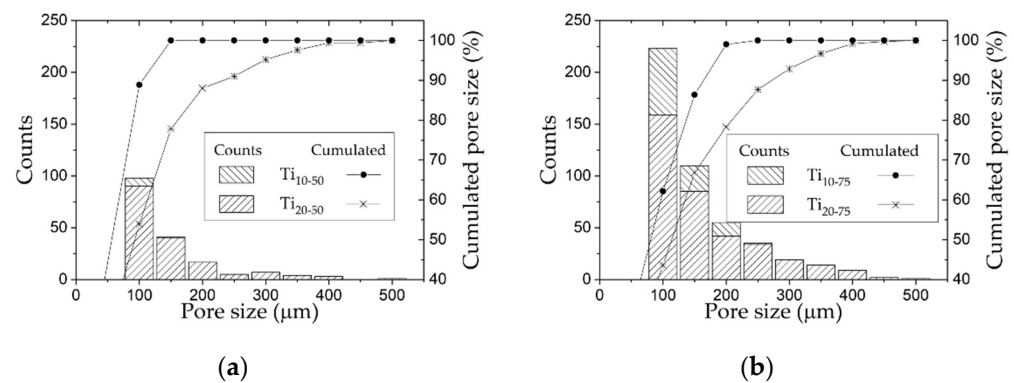


Figure 5. Pore size distribution: (a) Ti₁₀₋₅₀, Ti₂₀₋₅₀ (50% milled powder); (b) Ti₁₀₋₇₅, Ti₂₀₋₇₅ (75% milled powder).

To complement this analysis of the porosity size, Table 2 presents the image analysis data, showing the porosity percentage, the mean equivalent diameter, and the shape factor values expressed in terms of mean value \pm standard error. This value of porosity corresponds to that obtained only with the spacer. To do this, a criterion was applied where the pore size data was filtered, eliminating all the pores that were below 50 μm . Porosity percentage increases with the amount of milled powders, where the highest porosity was achieved for Ti₂₀₋₇₅ (~36%). Although the porosity obtained is less than the percentage of the added spacer, 50% NH_4HCO_3 , it is important to remember that the hot-pressing technique is used to obtain compacts with high densification. In this case, it is not only intended to introduce porosity in the consolidated titanium matrix, but it also seeks to improve the properties of the matrix and cycle times and reduce the temperature necessary for consolidation. The equivalent pore diameter was found in a range comprised between 84 ± 8 and 141 ± 4 μm . The ANOVA indicates that statistically significant differences exist in the pore size (p -value < 0.05), which confirms the suggested difference observed in the optical micrographs. There are influences of the milling time as well as of the amount of milled powder on the equivalent pore diameter in the specimens. By means of a Tukey's test, it was determined that the greatest significant difference of the equivalent diameter is about 60 μm . The pores shape factor was found in a range comprised between 0.70 and 0.80. In this case, the ANOVA indicates that there are no statistically significant differences (p -value > 0.05). This behavior is attributed to the deformation strengthening mechanism, where the milled powders have lost their ductile behavior; thus, the deformation is carried out mainly by the coarse particles. Another cause is the reduced size of the particles that have a greater surface energy, which results in a faster sintering that hinders the rearrangement of particles along the matrix.

3.3. Mechanical Characterization of Sintered Samples

Vickers microhardness distribution found in the consolidated samples with bimodal microstructure is shown in Figure 6. The mean values of microhardness measurements ranged between 589.4 ± 43.3 HV and 850.6 ± 62.2 HV, where the highest is found for Ti₂₀₋₇₅. These values exceed the c.p. Ti microhardness mean value (301 HV), being even higher than the reported values for the c.p. titanium components with a nanocrystalline structure or ultrafine-grained components consolidated by SPS [77], high-pressure torsion [78], or multi-pass ECAP [79], which are comprised in a range of 230 to 250 HV. They are closer to the ones reported for titanium components with a bimodal microstructure consolidated by SPS (660 to 853 HV) [45]. As it is observed, the microhardness distribution varies in function of the processing parameters: (i) when the amount of milled powder increases, the frequency of higher microhardness values increases, while (ii) the longer the milling time, the higher the mean value of microhardness. This increase in microhardness with the milling time and quantity of ground powder is mainly attributed to the accumulation of deformation energy [80], but also it could be influenced by the contamination with the

milling medium, which in turn depends on the time, intensity, atmosphere of milling, and the difference in the strength/hardness of the powders and milling medium [81]. Table 3 summarizes the statistical analysis of each microhardness distribution. From the ANOVA, it was determined that both parameters have a significant effect (p -value < 0.05) on the microhardness value. However, the amount of ground powder is more significant in increasing the microhardness, as shown in Table 3.

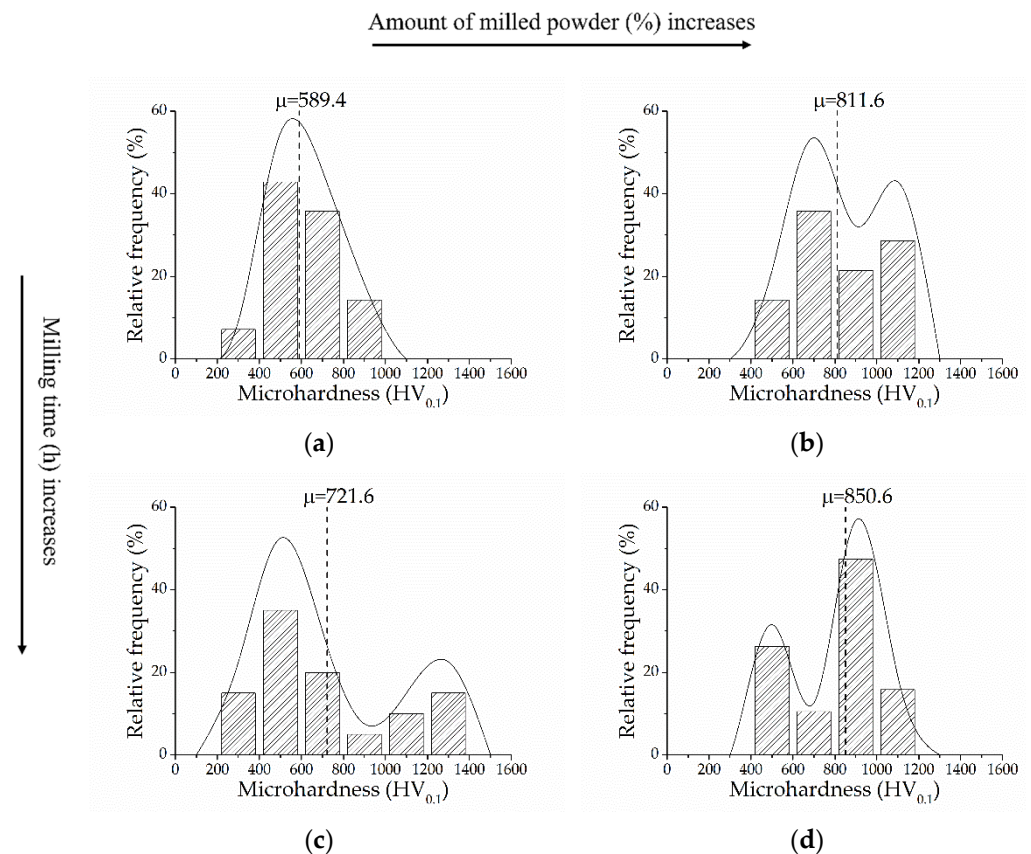


Figure 6. Vickers microhardness distribution for samples: (a) Ti₁₀₋₅₀; (b) Ti₁₀₋₇₅; (c) Ti₂₀₋₅₀; (d) Ti₂₀₋₇₅.

Table 3. Summary of statistical analysis of microhardness values (HV).

Sample	Milling Time (h)	Milled Powder (%)	Porosity (%)	Max. HV	Min. HV	Mean HV	Std. Error HV
c.p. Ti	0	0	-	430.8	232.1	312.9	11.2
Ti ₁₀₋₅₀	10	50	1.5 ± 0.4	890.3	374.5	589.4	43.3
Ti ₂₀₋₅₀	20	50	12.5 ± 3.8	1348.6	227.3	721.6	75.7
Ti ₁₀₋₇₅	10	75	13.2 ± 0.4	1109.4	516.7	811.6	52.5
Ti ₂₀₋₇₅	20	75	35.5 ± 1.5	1674.5	456.9	850.6	62.2

In addition, the mechanical properties estimated from the porosity and shape factor obtained from the image analysis are summarized in Table 4. These values are expressed in terms of mean value ± standard error. As it is observed, the elastic modulus decreases as the milling time and/or content of the milled powder increases, following the trend of increasing porosity. Yield strength has similar behavior due to the fact that it depends on the density value, and this is directly related to the porosity level. Nonetheless, the yield strength was estimated from a model which does not consider the strengthening effect due to deformation during the milling stage of the powders, or the presence of a bimodal structure, hence it is necessary to develop models in order to predict this behavior, which can be contrasted with experimental data.

Table 4. Estimated mechanical properties from bulk properties by means of Nielsen’s method [56] (E_p) and Jha’s correlation [58] ($\sigma_{y,f}$).

Sample	E_p (GPa)	$\sigma_{y,f}$ (MPa)
Ti ₁₀₋₅₀	106.0 ± 0.2	312.8
Ti ₂₀₋₅₀	80.9 ± 8.4	314.5
Ti ₁₀₋₇₅	79.4 ± 1.5	317.8
Ti ₂₀₋₇₅	41.8 ± 4.1	234.1

Previous studies have determined that the optimal porosity for an implant to efficiently stimulate bone ingrowth is in the range of 20–50% [82] with a pore size of 100–400 μm [83]. Furthermore, taking into account that the elastic modulus of the cortical bone is in a range from 20 to 25 GPa and that its ultimate tensile strength is about 195 MPa [3], it is ascertained that the Ti₂₀₋₇₅ specimen shows the characteristics suitable for bone replacement applications. The fatigue behavior of the specimens presented in this work is planned for future experiments, since metal fatigue [84] is one of the main causes of implants’ mechanical failure.

4. Conclusions

In this study, the porous titanium samples with a bimodal microstructure were successfully synthesized by hot pressing with NH_4HCO_3 as a space-holder. The effects of the milling time for obtaining fine powder as well as its amount over the microhardness and porosity were investigated. The conclusions are shown as follows:

- It has been determined that the processing route via the space-holder technique and hot pressing consolidation is effective in producing titanium samples with a porosity of 36% with a bimodal microstructure, whose microhardness has similar values to those obtained in nanocrystalline or ultrafine-grained microstructures synthesized by SPS. The microhardness value depends on the amount of fine powder that constitutes the matrix, and it is the result of deformation strengthening mechanisms and a small grain size;
- The obtained porosity in the titanium samples processed by this route depends on the milling time as well as the amount of fine powder due to the changes in particles size and distribution, deformation/rearrange capability of the powders, and the presence of agglomerates and contamination, all parameters which affect the compaction and sintering processes. However, when the milled powders for 20 h were used, larger pores were reached, whose sizes reached up to 400 μm . The Ti₂₀₋₇₅ sample presents appropriated mechanical properties for cortical bone replacement applications.

Author Contributions: Conceptualization, S.L., R.V.M. and Y.T.; methodology, C.A. and S.L.; validation, M.R.-V.; formal analysis, S.L., F.J.G., C.A., Y.T., R.C.-V., S.S. and C.S.; investigation, M.R.-V., R.V.M. and S.L.; resources, S.L., R.V.M., F.J.G. and Y.T.; writing—original draft preparation, R.C.-V. and S.S.; writing—review and editing, F.J.G., C.A. and S.L.; supervision, C.S. and R.V.M.; project administration, S.L.; funding acquisition, S.L., R.V.M., F.J.G. and Y.T. All authors have read and agreed to the published version of the manuscript.

Funding: This work was supported by the Agencia Nacional de Investigación y Desarrollo (ANID) of Chile government [grant number Fondecyt 11160865, and FONDEQUIP EQM130103 and EQM150101, and Scholarship Program/DOCTORADO/2021-21211274], and the Ministerio de Ciencia e Innovación of Spain under the grant PID2019-109371GB-I00.

Institutional Review Board Statement: Not applicable.

Informed Consent Statement: Not applicable.

Data Availability Statement: The data presented in this study are available on request from the corresponding author.

Acknowledgments: The authors thank the laboratory technicians Jesus Pinto at Universidad de Sevilla (Spain), Claudio Aravena and Gabriel Cornejo at Universidad Técnica Federico Santa María (Chile) for their support carrying out the microstructure characterization and mechanical testing.

Conflicts of Interest: The authors declare no conflict of interest.

References

1. Gao, C.; Peng, S.; Feng, P.; Shuai, C. Bone biomaterials and interactions with stem cells. *Bone Res.* **2017**, *5*, 17059. [[CrossRef](#)]
2. Geetha, M.; Singh, A.; Asokamani, R.; Gogia, A. Ti based biomaterials, the ultimate choice for orthopaedic implants—A review. *Prog. Mater. Sci.* **2009**, *54*, 397–425. [[CrossRef](#)]
3. Zhang, L.; Chen, L. A Review on Biomedical Titanium Alloys: Recent Progress and Prospect. *Adv. Eng. Mater.* **2019**, *21*, 1801215. [[CrossRef](#)]
4. Pałka, K.; Pokrowiecki, R. Porous Titanium Implants: A Review. *Adv. Eng. Mater.* **2018**, *20*, 1700648. [[CrossRef](#)]
5. Lascano, S.; Chávez-Vásquez, R.; Muñoz-Rojas, D.; Aristizabal, J.; Arce, B.; Parra, C.; Acevedo, C.; Orellana, N.; Reyes-Valenzuela, M.; Gotor, F.J.; et al. Graphene-coated Ti-Nb-Ta-Mn foams: A promising approach towards a suitable biomaterial for bone replacement. *Surf. Coat. Technol.* **2020**, *401*, 126250. [[CrossRef](#)]
6. Torres-Sanchez, C.; McLaughlin, J.; Bonallo, R. Effect of Pore Size, Morphology and Orientation on the Bulk Stiffness of a Porous Ti35Nb4Sn Alloy. *J. Mater. Eng. Perform.* **2018**, *27*, 2899–2909. [[CrossRef](#)]
7. Chino, Y.; Dunand, D.C. Directionally freeze-cast titanium foam with aligned, elongated pores. *Acta Mater.* **2008**, *56*, 105–113. [[CrossRef](#)]
8. Yook, S.-W.; Kim, H.-E.; Koh, Y.-H. Fabrication of porous titanium scaffolds with high compressive strength using camphene-based freeze casting. *Mater. Lett.* **2009**, *63*, 1502–1504. [[CrossRef](#)]
9. Han, C.; Li, Y.; Wang, Q.; Wen, S.; Wei, Q.; Yan, C.; Hao, L.; Liu, J.; Shi, Y. Continuous functionally graded porous titanium scaffolds manufactured by selective laser melting for bone implants. *J. Mech. Behav. Biomed. Mater.* **2018**, *80*, 119–127. [[CrossRef](#)] [[PubMed](#)]
10. Zhao, D.; Liang, H.; Han, C.; Li, J.; Liu, J.; Zhou, K.; Yang, C.; Wei, Q. 3D printing of a titanium-tantalum Gyroid scaffold with superb elastic admissible strain, bioactivity and in-situ bone regeneration capability. *Addit. Manuf.* **2021**, *47*, 102223. [[CrossRef](#)]
11. Orrù, R.; Licheri, R.; Locci, A.M.; Cincotti, A.; Cao, G. Consolidation/synthesis of materials by electric current activated/assisted sintering. *Mater. Sci. Eng. R Rep.* **2009**, *63*, 127–287. [[CrossRef](#)]
12. Ramskogler, C.; Warchomicka, F.; Mostofi, S.; Weinberg, A.; Sommitsch, C. Innovative surface modification of Ti6Al4V alloy by electron beam technique for biomedical application. *Mater. Sci. Eng. C* **2017**, *78*, 105–113. [[CrossRef](#)] [[PubMed](#)]
13. Saucedo, S.; Lascano, S.; Béjar, L.; Neves, G.O.; Chicardi, E.; Salvo, C.; Aguilar, C. Study of the Effect of the Floating Die Compaction on Mechanical Properties of Titanium Foams. *Metals* **2020**, *10*, 1621. [[CrossRef](#)]
14. Yamanoglu, R.; Bahador, A.; Kondoh, K. Fabrication Methods of Porous Titanium Implants by Powder Metallurgy. *Trans. Indian Inst. Met.* **2021**, *74*, 2555–2567. [[CrossRef](#)]
15. Niu, W.; Bai, C.; Qiu, G.B.; Wang, Q. Processing and properties of porous titanium using space holder technique. *Mater. Sci. Eng. A* **2009**, *506*, 148–151. [[CrossRef](#)]
16. Lascano, S. *Obtención y Caracterización de Ti c.p. Poroso Para Aplicaciones Biomédicas*; Universidad del Norte: Barranquilla, Columbia, 2012.
17. Rodríguez-Contreras, A.; Punset, M.; Calero, J.A.; Gil, F.J.; Ruperez, E.; Manero, J.M. Powder metallurgy with space holder for porous titanium implants: A review. *J. Mater. Sci. Technol.* **2021**, *76*, 129–149. [[CrossRef](#)]
18. Torres, Y.; Rodríguez, J.A.; Arias, S.; Echeverry, M.; Robledo, S.; Amigó, V.; Pavón, J.J. Processing, characterization and biological testing of porous titanium obtained by space-holder technique. *J. Mater. Sci.* **2012**, *47*, 6565–6576. [[CrossRef](#)]
19. Abhash, A.; Singh, P.; Kumar, R.; Pandey, S.; Sathaiyah, S.; Md. Shafeeq, M.; Mondal, D.P. Effect of Al addition and space holder content on microstructure and mechanical properties of Ti2Co alloys foams for bone scaffold application. *Mater. Sci. Eng. C* **2020**, *109*, 110600. [[CrossRef](#)]
20. Abhash, A.; Singh, P.; Muchhala, D.; Kumar, R.; Gupta, G.K.; Mondal, D.P. Research into the change of macrostructure, microstructure and compressive deformation response of Ti6Al2Co foam with sintering temperatures and space holder contents. *Mater. Lett.* **2020**, *261*, 126997. [[CrossRef](#)]
21. Civantos, A.; Giner, M.; Trueba, P.; Lascano, S.; Montoya-García, M.-J.; Arévalo, C.; Vázquez, M.Á.; Allain, J.P.; Torres, Y. In vitro bone cell behavior on porous titanium samples: Influence of porosity by loose sintering and space holder techniques. *Metals* **2020**, *10*, 696. [[CrossRef](#)]
22. Gupta, J.; Ghosh, S.; Aravindan, S. Effect of Mo and space holder content on microstructure, mechanical and corrosion properties in Ti6AlxMo based alloy for bone implant. *Mater. Sci. Eng. C* **2021**, *123*, 111962. [[CrossRef](#)] [[PubMed](#)]
23. Surace, R.; Filippis, L.A.C.D.; Ludovico, A.D.; Boghetich, G. Influence of processing parameters on aluminium foam produced by space holder technique. *Mater. Des.* **2009**, *30*, 1878–1885. [[CrossRef](#)]
24. Torres, Y.; Pavón, J.J.; Rodríguez, J.A. Processing and characterization of porous titanium for implants by using NaCl as space holder. *J. Mater. Proc. Technol.* **2012**, *212*, 1061–1069. [[CrossRef](#)]

25. Mansourighasri, A.; Muhamad, N.; Sulong, A.B. Processing titanium foams using taipoca starch as a space holder. *J. Mater. Proc. Technol.* **2012**, *212*, 83–89. [[CrossRef](#)]
26. Jakubowicz, J.; Adamek, G.; Dewidar, M. Titanium foam made with saccharose as a space holder. *J. Porous Mater.* **2013**, *20*, 1137–1141. [[CrossRef](#)]
27. Esen, Z.; Bor, S. Characterization of Ti-6Al-4V alloy foams synthesized by space holder technique. *Mater. Sci. Eng. A* **2011**, *528*, 3200–3209. [[CrossRef](#)]
28. Chen, Y.; Frith, J.E.; Dehghan-Manshadi, A.; Attar, H.; Kent, D.; Soro, N.D.M.; Bermingham, M.J.; Dargusch, M.S. Mechanical properties and biocompatibility of porous titanium scaffolds for bone tissue engineering. *J. Mech. Behav. Biomed. Mater.* **2017**, *75*, 169–174. [[CrossRef](#)]
29. Lai, T.; Xu, J.-L.; Xiao, Q.-F.; Tong, Y.-X.; Huang, J.; Zhang, J.-P.; Luo, J.-M.; Liu, Y. Preparation and characterization of porous NiTi alloys synthesized by microwave sintering using Mg space holder. *Trans. Nonferrous Met. Soc. China* **2021**, *31*, 485–498. [[CrossRef](#)]
30. Manonukul, A.; Muenya, N.; Léaux, F.; Amaranan, S. Effects of replacing metal powder with powder space holder on metal foam produced by metal injection moulding. *J. Mater. Proc. Technol.* **2010**, *210*, 529–535. [[CrossRef](#)]
31. Li, B.-q.; Li, Z.-q.; Lu, X. Effect of sintering processing on property of porous Ti using space holder technique. *Trans. Nonferrous Met. Soc. China* **2015**, *25*, 2965–2973. [[CrossRef](#)]
32. Chen, Y.; Frith, J.E.; Dehghan-Manshadi, A.; Kent, D.; Bermingham, M.; Dargusch, M. Biocompatible porous titanium scaffolds produced using a novel space holder technique. *J. Biomed. Mater. Res. Part B Appl. Biomater.* **2018**, *106*, 2796–2806. [[CrossRef](#)]
33. Guden, M.; Celik, E.; Akar, E.; Cetiner, S. Compression testing of a sintered Ti6Al4V powder compact for biomedical applications. *Mater. Caract.* **2005**, *54*, 399–408. [[CrossRef](#)]
34. Bafti, H.; Habibolahzadeh, A. Production of aluminum foam by spherical carbamide space holder technique-processing parameters. *Mater. Des.* **2010**, *31*, 4122–4129. [[CrossRef](#)]
35. Arifvianto, B.; Leeftang, M.A.; Zhou, J. The compression behaviors of titanium/carbamide powder mixtures in the preparation of biomedical titanium scaffolds with the space holder method. *Powder Technol.* **2015**, *284*, 112–121. [[CrossRef](#)]
36. Lascano, S.; Arévalo, C.; Montealegre-Melendez, I.; Muñoz, S.; Rodriguez-Ortiz, J.A.; Trueba, P.; Torres, Y. Porous Titanium for Biomedical Applications: Evaluation of the Conventional Powder Metallurgy Frontier and Space-Holder Technique. *Appl. Sci.* **2019**, *9*, 982. [[CrossRef](#)]
37. Abbasi, N.; Hamlet, S.; Love, R.M.; Nguyen, N.-T. Porous scaffolds for bone regeneration. *J. Sci. Adv. Mater. Devices* **2020**, *5*, 1–9. [[CrossRef](#)]
38. Suryanarayana, C.; Al-Aqueeli, N. Mechanically alloyed nanocomposites. *Prog. Mater. Sci.* **2013**, *58*, 383–502. [[CrossRef](#)]
39. Misra, D.K.; Rakshit, R.K.; Singh, M.; Shukla, P.K.; Chaturvedi, K.M.; Sivaiah, B.; Gahtori, B.; Dhar, A.; Sohn, S.W.; Kim, W.T.; et al. High yield strength bulk Ti based bimodal ultrafine eutectic composites with enhanced plasticity. *Mater. Des.* **2014**, *58*, 551–556. [[CrossRef](#)]
40. Kang, L.; Yang, C. A Review on High-Strength Titanium Alloys: Microstructure, Strengthening, and Properties. *Adv. Eng. Mater.* **2019**, *21*, 1801359. [[CrossRef](#)]
41. Long, Y.; Wang, T.; Zhang, H.Y.; Huang, X.L. Enhanced ductility in a bimodal ultrafine-grained Ti-6Al-4V alloy fabricated by high energy ball milling and spark plasma sintering. *Mater. Sci. Eng. A* **2014**, *608*, 82–89. [[CrossRef](#)]
42. Okulov, I.V.; Bönisch, M.; Kühn, U.; Skrotzki, W.; Eckert, J. Significant tensile ductility and toughness in an ultrafine-structured Ti68.8Nb13.6Co6Cu5.1Al6.5 bi-modal alloy. *Mater. Sci. Eng. A* **2014**, *615*, 457–463. [[CrossRef](#)]
43. Vajpai, S.K.; Sawangrat, C.; Yamaguchi, O.; Cluca, O.P.; Ameyama, K. Effect of bimodal harmonic structure design on the deformation behaviour and mechanical properties of Co-Cr-Mo alloy. *Mater. Sci. Eng. C* **2016**, *58*, 1008–1015. [[CrossRef](#)]
44. Zheng, Y.; Yao, X.; Su, Y.; Zhang, D.L. High strength titanium with a bimodal microstructure fabricated by thermomechanical consolidation of a nanocrystalline TiH₂ powder. *Mater. Sci. Eng. A* **2017**, *686*, 11–18. [[CrossRef](#)]
45. Yang, C.; Ni, S.; Liu, Y.; Song, M. Effects of sintering parameters on the hardness and microstructures of bulk bimodal titanium. *Mater. Sci. Eng. A* **2015**, *625*, 264–270. [[CrossRef](#)]
46. Chang, S.; Doremus, R.H.; Schadler, L.S.; Siegel, R.W. Hot-Pressing of Nano-Size Alumina Powder and the Resulting Mechanical Properties. *Int. J. Appl. Ceram. Technol.* **2004**, *1*, 172–179. [[CrossRef](#)]
47. Dong, S.; Jiang, D.; Tan, S.; Guo, J. Preparation and characterization of nano-structured monolithic SiC and Si₃N₄/SiC composite by hot isostatic pressing. *J. Mater. Sci. Lett.* **1997**, *16*, 1080–1083. [[CrossRef](#)]
48. McCusker, L.; Dreele, R.V.; Cox, D.; Louër, D.; Scardi, P. Rietveld refinement guidelines. *J. Appl. Crystallogr.* **1999**, *32*, 36–50. [[CrossRef](#)]
49. Lopez, E.I.P.; Saint-Laurence, P.I.M.; Ramirez, C.E.A.; Gomez, L.B.; Flores, A.M.; Jimenez, F.D.L.C.; López, I.A. Estudio de perfiles de difracción de rayos X de una aleación Ti-13Ta-3Sn obtenida por aleado mecánico. *Matéria* **2020**, *25*. [[CrossRef](#)]
50. Hernández-Nava, E.; Mahoney, P.; Smith, C.J.; Donoghue, J.; Todd, I.; Tammis-Williams, S. Additive manufacturing titanium components with isotropic or graded properties by hybrid electron beam melting/hot isostatic pressing powder processing. *Sci. Rep.* **2019**, *9*, 4070. [[CrossRef](#)]
51. Petrovskiy, P.; Sova, A.; Doubenskaia, M.; Smurov, I. Influence of hot isostatic pressing on structure and properties of titanium cold-spray deposits. *Int. J. Adv. Manuf. Technol.* **2019**, *102*, 819–827. [[CrossRef](#)]
52. ASTM F1877-16; *Standard Practice for Characterization of Particles*; ASTM International: West Conshohocken, PA, USA, 2016.
53. ASTM E2651-19; *Standard Guide for Powder Particle Size Analysis*; ASTM International: West Conshohocken, PA, USA, 2019.

54. ISO 13314:2011; *Mechanical Testing of Metals-Ductility Testing-Compression Test for Porous and Cellular Metals*; ISO: Geneva, Switzerland, 2011.
55. ASTM E9-19; *Standard Test Methods of Compression Testing of Metallic Materials at Room Temperature*; ASTM International: West Conshohocken, PA, USA, 2019.
56. Nielsen, L.F. Elasticity and Damping of Porous Materials and Impregnated Materials. *J. Am. Ceram. Soc.* **1984**, *67*, 93–98. [[CrossRef](#)]
57. Li, Y.; Yang, C.; Zhao, H.; Qu, S.; Li, X.; Li, Y. New developments of Ti-based alloys for biomedical applications. *Materials* **2014**, *7*, 1709–1800. [[CrossRef](#)] [[PubMed](#)]
58. Jha, N.; Mondal, D.P.; Majumdar, J.D.; Badkul, A.; Jha, A.K.; Khare, A.K. Highly porous open cell Ti-foam using NaCl as temporary space holder through powder metallurgy route. *Mater. Des.* **2013**, *47*, 810–819. [[CrossRef](#)]
59. Torres, Y.; Lascano, S.; Bris, J.; Pavón, J.; Rodriguez, J.A. Development of porous titanium for biomedical applications: A comparison between loose sintering and space-holder techniques. *Mater. Sci. Eng. C* **2014**, *37*, 148–155. [[CrossRef](#)] [[PubMed](#)]
60. Soufiani, A.M.; Karimzadeh, F.; Enayati, M.H. Formation mechanism and characterization of nanostructured Ti6Al4V alloy prepared by mechanical alloying. *Mater. Des.* **2012**, *37*, 152–160. [[CrossRef](#)]
61. Guzzo, P.L.; Marino, F.B.d.B.; Soares, B.R.; Santos, J.B. Evaluation of particle size reduction and agglomeration in dry grinding of natural quartz in a planetary ball mill. *Powder Technol.* **2020**, *368*, 149–159. [[CrossRef](#)]
62. Suryanarayana, C. Mechanical alloying and milling. *Prog. Mater. Sci.* **2001**, *46*, 1–184. [[CrossRef](#)]
63. Salvo, C.; Aguilar, C.; Cardoso-Gil, R.; Medina, A.; Bejar, L.; Mangalaraja, R.V. Study on the microstructural evolution of Ti-Nb based alloy obtained by high-energy ball milling. *J. Alloy. Compd.* **2017**, *720*, 254–263. [[CrossRef](#)]
64. Chicardi, E.; García-Garrido, C.; Sayagués, M.J.; Torres, Y.; Amigó, V.; Aguilar, C. Development of a novel fcc structure for an amorphous-nanocrystalline Ti-33Nb-4Mn (at.%) ternary alloy. *Mater. Charact.* **2018**, *135*, 46–56. [[CrossRef](#)]
65. Aguilar, C.; Pio, E.; Medina, A.; Mangalaraja, R.V.; Salvo, C.; Alfonso, I.; Guzmán, D.; Bejar, L. Structural Study of Novel Nanocrystalline fcc Ti-Ta-Sn Alloy. *Metall. Mater. Trans. A* **2019**, *50*, 2061–2065. [[CrossRef](#)]
66. Tejeda-Ochoa, A.; Kametani, N.; Carreño-Gallardo, C.; Ledezma-Sillas, J.E.; Adachi, N.; Todaka, Y.; Herrera-Ramirez, J.M. Formation of a metastable fcc phase and high Mg solubility in the Ti-Mg system by mechanical alloying. *Powder Technol.* **2020**, *374*, 348–352. [[CrossRef](#)]
67. Aguilar, C.; Pio, E.; Medina, A.; Martínez, C.; Sancy, M.; Guzman, D. Evolution of synthesis of FCC nanocrystalline solid solution and amorphous phase in the Ti-Ta based alloy by high milling energy. *J. Alloy. Compd.* **2021**, *854*, 155980. [[CrossRef](#)]
68. Lange, F.F. Densification of powder compacts: An unfinished story. *J. Eur. Ceram. Soc.* **2008**, *28*, 1509–1516. [[CrossRef](#)]
69. Ivasishin, O.M.; Savvakina, D.G.; Froes, F.H.; Mokson, V.C.; Bondareva, K.A. Synthesis of the Ti-6Al-4V alloy having low residual porosity by powder metallurgy method. *Powder Metall. Met. Ceram.* **2002**, *41*, 382–390. [[CrossRef](#)]
70. Robertson, I.M.; Schaffer, G.B. Some Effects of Particle Size on the Sintering of Titanium and a Master Sintering Curve Model. *Metall. Mater. Trans. A* **2009**, *40*, 1968–1979. [[CrossRef](#)]
71. Qian, M. Cold compaction and sintering of titanium and its alloys for near-net-shape or preform fabrication. *Int. J. Powder Metall.* **2010**, *46*, 29–44.
72. Robertson, I.M.; Schaffer, G.B. Review of densification of titanium based powder systems in press and sinter processing. *Powder Metall.* **2010**, *53*, 146–162. [[CrossRef](#)]
73. Lange, F. De-sintering, A phenomenon concurrent with densification within powder compacts: A review. In *Sintering Technology*, 1st ed.; Marcel Dekker, Inc.: New York, NY, USA, 1996; pp. 1–12.
74. Gupta, N.; Basu, B. Hot pressing and spark plasma sintering techniques of intermetallic matrix composites. In *Intermetallic Matrix Composites*, 1st ed.; Mitra, R., Ed.; Elsevier: Duxford, UK, 2018; pp. 243–302.
75. Dirras, G.; Gubicza, J.; Ramtani, S.; Bui, Q.H.; Szilágyi, T. Microstructure and mechanical characteristics of bulk polycrystalline Ni consolidated from blends of powders with different particle size. *Mater. Sci. Eng. A* **2010**, *527*, 1206–1214. [[CrossRef](#)]
76. Singer, A.; Barakat, Z.; Mohapatra, S.; Mohapatra, S.S. Chapter 13–Nanoscale Drug-Delivery Systems: In Vitro and In Vivo Characterization. In *Nanocarriers for Drug Delivery*; Mohapatra, S.S., Ranjan, S., Dasgupta, N., Mishra, R.K., Thomas, S., Eds.; Elsevier: Amsterdam, The Netherlands, 2019; pp. 395–419.
77. Ertoter, O.; Topping, T.D.; Li, Y.; Moss, W.; Lavernia, E.J. Nanostructured Ti Consolidated via Spark Plasma Sintering. *Metall. Mater. Trans. A* **2011**, *42*, 964–973. [[CrossRef](#)]
78. Edalati, K.; Daio, T.; Arita, M.; Lee, S.; Horita, Z.; Togo, A.; Tanaka, I. High-pressure torsion of titanium at cryogenic and room temperatures: Grain size effect on allotropic phase transformations. *Acta Mater.* **2014**, *68*, 207–213. [[CrossRef](#)]
79. Hajizadeh, K.; Eghbali, B.; Topolski, K.; Kurzydowski, K.J. Ultra-fine grained bulk CP-Ti processed by multi-pass ECAP at warm deformation region. *Mat. Chem. Phys.* **2014**, *143*, 1032–1038. [[CrossRef](#)]
80. Suryanarayana, C.; Klassen, T.; Ivanov, E. Synthesis of nanocomposites and amorphous alloys by mechanical alloying. *J. Mater. Sci.* **2011**, *46*, 6301–6315. [[CrossRef](#)]
81. Alijani, F.; Amini, R.; Ghaffari, M.; Alizadeh, M.; Okyay, A.K. Effect of milling time on the structure, micro-hardness, and thermal behavior of amorphous/nanocrystalline TiNiCu shape memory alloys developed by mechanical alloying. *Mater. Des.* **2014**, *55*, 373–380. [[CrossRef](#)]
82. Vasconcellos, L.; Leite, D.; Oliveira, F.; Carvalho, Y.; Cairo, C. Evaluation of bone ingrowth into porous titanium implants: Histomorphometric analysis in rabbits. *Implantol. Braz. Oral. Res.* **2010**, *24*, 399. [[CrossRef](#)]

-
83. Hollister, S. Scaffold Design and Manufacturing: From Concept to Clinic. *Adv. Mater.* **2009**, *21*, 3330. [[CrossRef](#)]
 84. Shemtov-Yona, K.; Rittel, D. Fatigue of Dental Implants: Facts and Fallacies. *Dent. J.* **2016**, *4*, 16. [[CrossRef](#)] [[PubMed](#)]